Journal of Materials Chemistry C

ROYAL SOCIETY OF CHEMISTRY

PAPER

View Article Online
View Journal | View Issue

Cite this: J. Mater. Chem. C, 2025, 13, 2229

Colossal barocaloric effect in fatty acid methyl esters†

Diyi Fu,‡[a] Xiu Su,‡[ab] Haoyu Wang,‡[cd] Zhenxing Li,[b] Qiang Zheng,*[a] Jun Shen,[b] Bing Li[cd] and Juan Du*[a]

Received 15th August 2024,
Accepted 20th November 2024

DOI: 10.1039/d4tc03483j

rsc.li/materials-c

The barocaloric effect is a green refrigeration technology, offering a more environmentally friendly alternative to conventional gas compression refrigeration. The barocaloric effect is induced by pressure in phase change materials, and in which high entropy change and adiabatic temperature change were obtained. Here, a colossal barocaloric effect was discovered in solid–liquid transition of fatty acid methyl esters (FAMEs). In methyl palmitate, the isothermal entropy change can reach as high as 707 J kg^{-1} K^{-1} under a low pressure of 80 MPa at 311 K; in methyl stearate, the isothermal entropy change can reach up to 680 J kg^{-1} K^{-1} under a pressure of 60 MPa at 308 K. These values are comparable to those of traditional refrigeration materials, such as R314a. The calculated adiabatic temperature change is 22 K for methyl palmitate and 13 K for methyl stearate. Raman spectroscopy indicates that unloading pressure to the liquid phase facilitates the formation of *gauche* bonds and the formation of solid–liquid phase transformation, which results in a larger configuration entropy change. This work provides a new candidate for solid–liquid transition materials in the practical application of barocaloric effect refrigeration.

Introduction

Refrigeration technology is becoming an increasingly important part of our global village, including food manufacture, air conditioning, aerospace, *etc.*[1] Due to the increasing demands for human refrigeration, it is estimated that 20–25% of the world's electricity is consumed in refrigeration technology.[2,3] Nowadays, thousands of refrigeration applications mainly utilize gas compression refrigeration technology, which brings huge convenience to our modern life.[4,5] However, this technology has many drawbacks, for instance, the greenhouse effect and high energy consumption.[6,7] Significantly, emissions from gas compression technology in which hydrochlorofluorocarbons (HCFCs) were applied as refrigerants are thousands of times more harmful to the ozone layer than CO_2, thus aggravating global warming.[8,9] Therefore, in order to reduce greenhouse gas emissions and protect our environment, it is an urgent task to find an environmentally friendly cooling technology to replace high-emission technology.[10] Luckily, caloric effect refrigeration technology is developing rapidly, which is the most promising refrigeration technology to replace traditional ones.[11,12]

Caloric effects can be categorized as magnetocaloric effects,[13–15] elastocaloric effects,[16] electrocaloric effects[17–19] and barocaloric effects (BCEs),[20–24] which are driven by a magnetic field, uniaxial stress field, electric field and hydrostatic pressure, respectively. For the barocaloric effect, temperature change and entropy change can be obtained during phase transition under external pressure, which is not system-selective unlike the other caloric effects.[25] So far, BCE has been observed in many kinds of materials including hybrid organic–inorganic compounds,[26] ferroelectrics,[27] ferroelastics,[28] thermoelectrics,[29] plastic crystals, frustrated antiferromagnets, spin-crossover complexes,[30] and so forth. Recently, a colossal barocaloric effect was found in plastic crystals, which was considered as a remarkable milestone in barocaloric materials because of the increase in entropy change from dozens of J kg^{-1} K^{-1} for conventional barocaloric materials to several hundreds of J kg^{-1} K^{-1} in plastic crystals. For instance, the entropy change of plastic crystal neopentyl glycol (NPG) can reach 389 J kg^{-1} K^{-1}, which is approximately one order higher than conventional barocaloric materials, and even comparable to the commercial refrigerants (such as R134a).[31] Recently, it was shown that metal–organic frameworks (MOFs) with breathing transitions have huge temperature variations under low pressure.

[a] Institute of Materials, School of Materials Science and Engineering, Shanghai University, Shanghai, 200444, People's Republic of China. E-mail: qiangzheng616@hotmail.com, jdu-case@hotmail.com
[b] Department of Energy and Power Engineering, School of Mechanical Engineering, Beijing Institute of Technology, Beijing 100081, People's Republic of China
[c] Shenyang National Laboratory for Materials Science, Institute of Metal Research, Chinese Academy of Sciences, 72 Wenhua Road, Shenyang, Liaoning 110016, People's Republic of China
[d] School of Materials Science and Engineering, University of Science and Technology of China, 72 Wenhua Road, Shenyang, Liaoning 110016, People's Republic of China

† Electronic supplementary information (ESI) available. See DOI: https://doi.org/10.1039/d4tc03483j

‡ These three authors contributed equally to this work.

For example, $Zn_2(bdc)_2(bpy)$ can expand the operating temperature range from 273 to 333 K under ultra low pressure (26 bar), and can be explored as a promising material in the future.[32] However, the biggest challenge for most BCE materials is to overcome the high driving pressure before the real barocaloric refrigeration application.

The materials will undergo a significant configurational change with a tremendous entropy change when their states were changed, such as from solid state to liquid state. And this is similar to gas–liquid transition, which has a huge entropy change.[33,34] Moreover, the liquid–solid transition (L–S-T) materials have a giant volume change caused by density variation. Therefore, the L–S-T materials are sensitive to pressure and suitable for the barocaloric effect.[35,36]

Fatty acid methyl esters (FAMEs) as a kind of typical L–S-T material are commonly applied for phase change energy storage. Methyl palmitate (MP) and methyl stearate (MS) have many advantages, including high latent heat of phase transition, strong chemical stability and low cost. And the high latent heat of the phase transition means better barocaloric effect. Here, the colossal barocaloric effect associated with methyl palmitate (MP) and methyl stearate (MS) was reported. Both of them undergo a solid-to-liquid phase transition near room temperature. The maximum entropy changes $\Delta S_{P_0 \to P}$ are 707 J kg^{-1} K^{-1} at 80 MPa for MP and 680 J kg^{-1} K^{-1} at 60 MPa for MS, respectively. And an effective refrigeration capacity of 1921 J kg^{-1} for MP and 4760 J kg^{-1} for MS can also be obtained. Moreover, these outstanding BCEs of FAMEs make them excellent candidate materials for barocaloric refrigeration applications.

Experimental details

The methyl palmitate (MP) (99% purity) and methyl stearate (MS) (99% purity) fatty acid esters were commercially available from Aladdin Inc. The raw materials were used as received from suppliers without any further purification. A high-pressure differential scanning calorimeter (μDSC7, Setaram) was used to collect heat flow data as a function of temperature at a constant hydrostatic pressure. The sample, with a mass of 18.8 mg for methyl palmitate and 12.6 mg for methyl stearate, respectively, was enclosed in a high-pressure Hastelloy vessel, and an empty vessel served as a standard. The heat flow of FAMEs was measured between 271 K and 333 K for hydrostatic pressures of 0.1, 20, 40, 60, 80 and 100 MPa. The heating and cooling rates were set to 1 K min^{-1}. The phase transition temperature was determined as the temperature at which the heat flow reached its maximum value. Subsequently, the entropy change at a constant pressure was calculated by integrating the thermal flow within a specific temperature interval. After subtracting the baseline, the entropy change at constant pressure ΔSP was calculated by integrating the thermal flow Q (P, T) within the temperature interval between T_1 and T_2. The specific heat capacity data at atmospheric pressure was measured between 270 and 330 K by DSC at a heating rate of 1 K min^{-1}. The $C_p(T)$ value at the corresponding phase transition temperature was used to calculate the adiabatic temperature.

Raman spectra were acquired utilizing a commercial Raman system (Horiba Labram HR Evolution) with a helium-neon laser (λ = 532 nm) incident at a normal angle. The samples were irradiated by the laser beam through a ×50 objective (numerical aperture 0.6), producing a beam diameter of approximately 1 μm. To maintain a controlled temperature environment, the sample was placed within a continuous-flow liquid-nitrogen cryostat, and temperature regulation was achieved using a calibrated Linkam heating–cooling stage equipped with a thermocouple attached to the sample holder. Raman spectra of MP and MS were measured at different temperatures. The typical frequency range was 50–3000 cm^{-1}, and LabSpec 5 was used to analyze all of the raw data.

Results and discussion

High-pressure differential scanning calorimetry

The solid–liquid phase transitions were also investigated by differential scanning calorimetry, and the heat flow peak changes were recorded in dQ/dT (Q is heat and T is temperature) during heating and cooling under ambient pressure. The heat flow data of MP and MS are plotted in Fig. 1, respectively. T_0 is defined as the starting transition temperature. Under atmospheric pressure, these FAMEs exhibit a solid–liquid transition at T_0 = 303 K for MP and at T_0 = 310 K for MS on heating. By integrating the DSC curves, the latent heat Q_0 during the

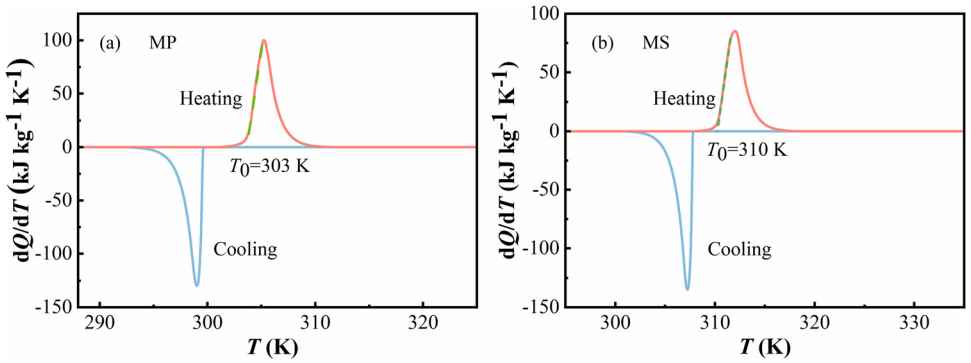

Fig. 1 dQ/dT curves of (a) methyl palmitate (MP) and (b) methyl stearate (MS).

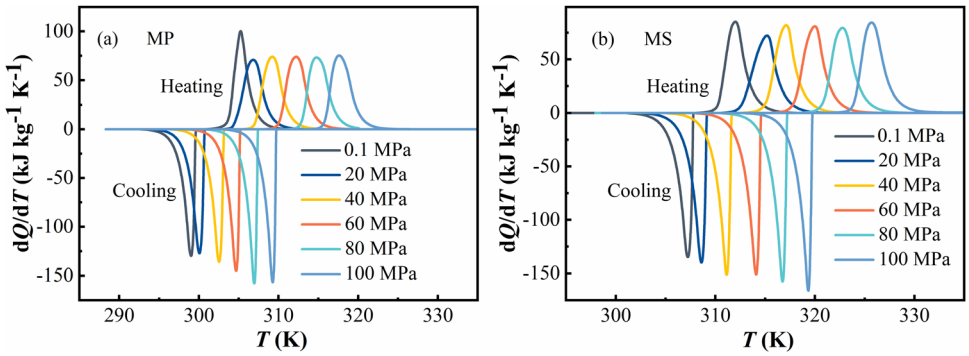

Fig. 2 dQ/dT curves of FAMEs at different pressures P = 0.1, 20, 40, 60, and 80 MPa. (a) Methyl palmitate (MP) and (b) methyl stearate (MS).

heating and cooling process can be determined to be 216 J kg^{-1} K^{-1} and 207 J kg^{-1} K^{-1} for MP and 206 J kg^{-1} K^{-1} and 209 J kg^{-1} K^{-1} for MS, respectively. Generally, the temperature of the transition finish on heating and the start and finish temperature for transition on cooling can be influenced by the temperature ramp rate. However, the temperature ramp rate has nominally no effect on the starting transition temperature T_0 on heating and $|Q_0| = \left|\int_{T_1}^{T_2} \frac{dQ}{dT} dT\right|$ across the solid–liquid transition (see Fig. S1 in the ESI†).[20,23]

As shown in Fig. 2, according to the determination of dQ/dT at different pressures, the transition temperatures of both FAMEs obviously shifted to higher temperatures with the increase of pressures. The phase transition temperature can be elevated by 10–15 K when the pressure reaches 100 MPa for MP and MS.

Barocaloric effect in fatty acid methyl esters

The entropy change of solid–liquid phase transitions of MP and MS under different pressures was obtained by eqn (S1) in the ESI.† Fig. 3 gives the entropy changes ΔS_{LS} in L–S-T during heating and cooling at P = 0.1, 20, 40, 60, 80 and 100 MPa. It can be seen in Fig. 3a and c that during the heating process both FAMEs showed a tendency of maximum entropy change ΔS_{LS} as the pressure increased, except MP at 20 MPa. It can be seen that the maximum entropy changes are about 726 J kg^{-1} K^{-1} and 714 J kg^{-1} K^{-1} for MP and MS under 100 MPa, respectively.

For the cooling process in Fig. 3b and d, the maximum entropy change ΔS_{LS} also increases with the increase of applied pressure. The maximum entropy changes are about 736 J kg^{-1} K^{-1} and 708 J kg^{-1} K^{-1} for MP and MS under 100 MPa, respectively. In contrast, entropy change was suppressed by pressure in other materials, which might contribute to the weak compressibility of

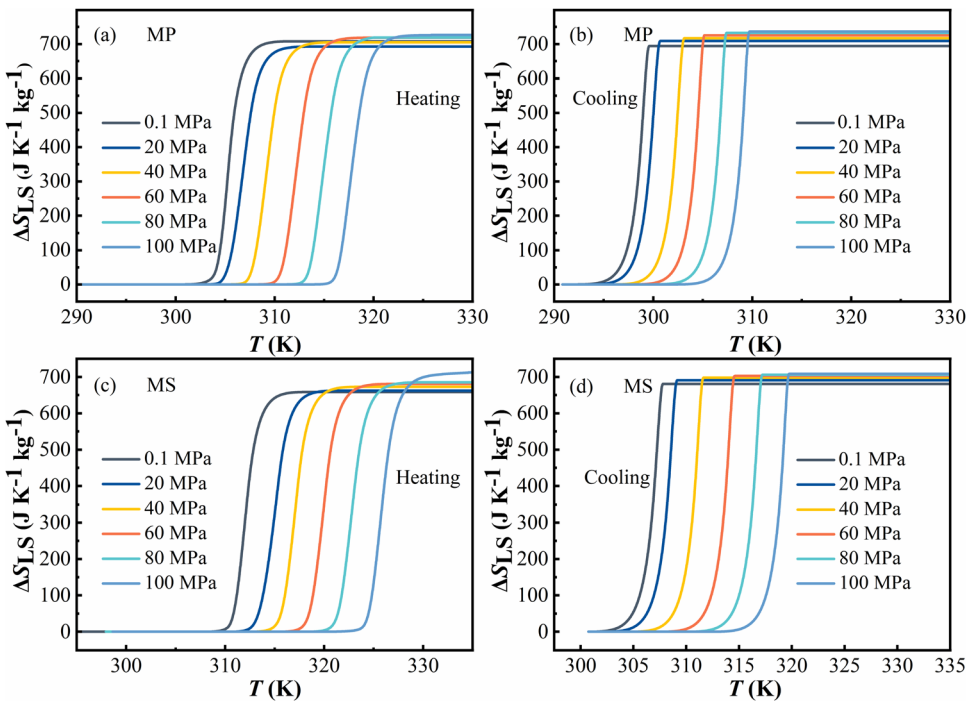

Fig. 3 Entropy changes ΔS_{LS} in L–S-T during heating and cooling processes at P = 0.1, 20, 40, 60, 80 and 100 MPa. (a) and (b) Methyl palmitate (MP) and (c) and (d) methyl stearate (MS).

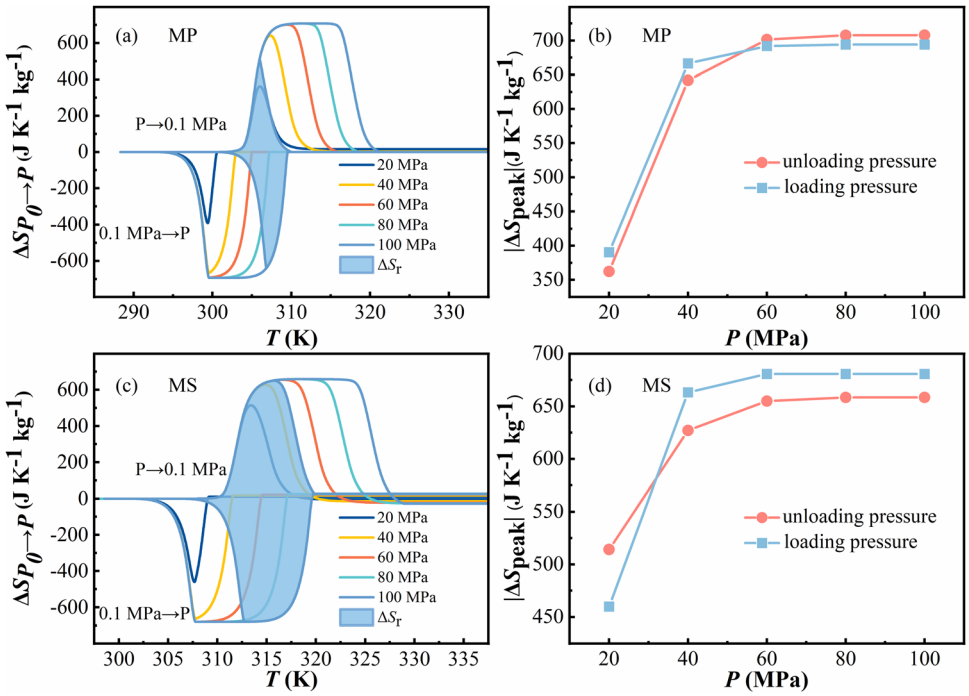

Fig. 4 Isothermal entropy changes $\Delta S_{P_0 \to P}$ from P = 0.1 MPa to 20, 40, 60, 80 and 100 MPa and reversible entropy change ΔS_r (shaded part) at 100 MPa and isothermal entropy change peak $|\Delta S_{Peak}|$ with pressure. (a) and (b) for MP; (c) and (d) for MS.

the FAMEs. As usual, the transition temperature shifts to higher temperature with the increase of pressure.

The isothermal entropy change at different pressures can be calculated by eqn (S2) in the ESI.† The pressure-induced entropy changes ($\Delta S_{P_0 \to P}$) are shown in Fig. 4 under different pressures. For MP, the maximum value of $\Delta S_{P_0 \to P}$ at 80 MPa is 707 J kg^{-1} K^{-1} at around 311 K for the loading pressure process and 694 J kg^{-1} K^{-1} at around 300 K for the unloading pressure process. For MS, the maximum value of $\Delta S_{P_0 \to P}$ at 60 MPa is 680 J kg^{-1} K^{-1} at around 308 K for the loading pressure process and 658 J kg^{-1} K^{-1} at around 317 K for the unloading pressure process, respectively. Reversible isothermal entropy change (ΔS_{rev}) is defined as the overlap of the $\Delta S_{P_0 \to P}$ curves during cooling and heating. As shown in Fig. 4, the maxima of ΔS_{rev} are about 641 J kg^{-1} K^{-1} for MP and 680 J kg^{-1} K^{-1} for MS under a pressure of 100 MPa.

Meanwhile, the peak of the isothermal entropy ΔS_{peak} is shown in Fig. 4b and d and it shows a positive tendency with pressure increasing. With the increase of pressure, the isothermal entropy ΔS_{peak} also increases and approaches saturation under a pressure of 80 MPa and 60 MPa for MP and MS, respectively.

According to the heat flow data, phase diagrams can be constructed, which were given in Fig. 5. dT/dP is defined as the phase boundary's slope.[37] Meanwhile, it's also an important indicator of barocaloric refrigerant materials. For MP, the dT/dP is 0.13 K MPa^{-1} on heating and 0.11 K MPa^{-1} on cooling within a pressure range of 0.1–100 MPa. Because of the larger slope while heating, the thermal hysteresis of MP is increased from 6 K at atmospheric pressure to 8 K at 100 MPa. Similarly, for MS, the dT/dP is 0.13 K MPa^{-1} on both heating and cooling when the pressure changes between 0.1 and 100 MPa, and its

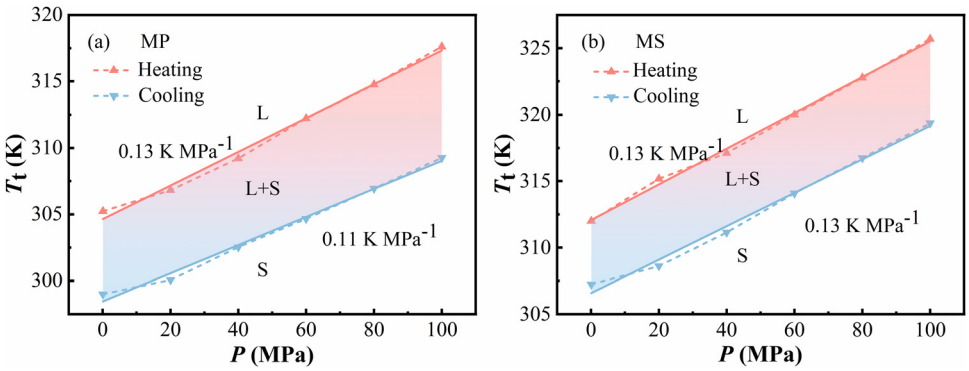

Fig. 5 Temperature-pressure diagram of L–S-T. (a) Methyl palmitate (MP) and (b) methyl stearate (MS).

Table 1 Comparison of the barocaloric performances of some classical barocaloric materials

Material	T_t (K)	ΔP (MPa)	dT_t/dP (K MPa^{-1})	$\Delta S^{max}_{P_0\rightarrow P}$ (J kg^{-1} K^{-1})	ΔT_{ad} (K)	T_{hys} (K)	Ref.
NPG $(CH_3)_2C(CH_2OH)_2$	300	91	0.13	384	16[a]	14	2
TRIS $(NH_2)C(CH_2OH)_3$	331	250	0.015	600	8	75	38
PG $(CH_3)C(CH_2OH)_3$	350	240	0.094	490[a]	10[a]	4	38
NPA $(CH_3)_3C(CH_2OH)$	211	260	0.12	290[a]	16[a]	20	38
$C_{16}H_{34}$	295	400	0.14	730[a]	58	—	33
$C_{18}H_{38}$	305	450	0.14	700[a]	50	—	33
Ortho-carborane	269	30	0.13	88	—	8	37
Meta-carborane	277	30	0.09	80.9	—	9	37
Para-carborane	297	30	0.17	106.2	—	11	37
AgI	407	250	0.14	60[a]	18	25	39
$(CH_3–(CH_2)_9)_2NH_2Cl$	316	100	0.19	400[a]	9.4	8	40
FAI	339	100	0.097	49.9[a]	24[esti]	5	41
$Fe_3(pz)_2(BH_3CN)_2$	318	100	0.2	200	—	47	30
$[Fe(L)_2](BF_4)_2$/PVC [L = 2,6 di(pyrazol-1-yl)pyridine]	255	450	0.1	168	49	—	42
$(CH_3–(CH_2)_8–NH_3)_2MnCl_4$	289	100	0.17	212[a]	10[a]	5.2	26
$(CH_3–(CH_2)_9–NH_3)_2MnCl_4$	306	100	—	250[a]	12[a]	9	26
$(DA)_2MnCl_4$ (DA = decylammonium)	308	50	0.225	248[a]	7[a]	1.4	43
$(NA)_2CuBr_4$ (NA = nonylammonium)	303.5	50	0.267	91.3[a]	9.4[a]	0.4	43
$C_{12}H_{26}O$	292	80	0.14	748[a]	22	6.6	21
C_{60}	257	410	0.172	42	16	2	44
$C_{10}H_{20}O_2$	296	300	0.2	600[a]	50	5	45
$C_{12}H_{24}O_2$	310	300	0.2	600[a]	50	4	45
$C_{14}H_{28}O_2$	321	300	0.2	600[a]	50	3	45
$Fe(L)(NCS)_2$	266	100	0.18	114[a]	15.9	1.5	46
$MnFe_{0.8+x}Ni_{1.2-x}SiGe_{0.5}$	310	100	—	43.72	—	19	47
R134a	310	1	—	520[a]	—	—	31
$CH_3(CH_2)_{14}CO_2CH_3$	299	100	0.13	707	22[esti]	6	This work
$CH_3(CH_2)_{16}CO_2CH_3$	307	100	0.13	680	13[esti]	5	This work

[a] Is reversible value and esti is the estimated value. Note: T_t is the transition temperature for cooling, ΔP is the applied pressure, T_{hys} is the thermal hysteresis at atmospheric pressure

hysteresis is kept at 5 K. A few parameters of barocaloric performances of the typical BCE materials are listed in Table 1, including T_t, dT_t/dP, $\Delta S^{max}_{P_0\rightarrow P}$, ΔT_{hys}, *etc.* In summary, both MP and MS have a huge entropy change and a good pressure sensitivity compared with other typical BCE materials, which indicated that they are promising candidate materials for barocaloric refrigeration applications.

The adiabatic temperature is an important indicator of barocaloric materials, which can be estimated from isothermal entropy change by an indirect method as follows:

$$\Delta T_{ad} = \frac{|\Delta S| T_t}{C_p} \quad (1)$$

where C_p is the specific heat capacity at atmospheric pressure. For MP, the maximum value of $\Delta S_{P_0\rightarrow P}$ is 707 J kg^{-1} K^{-1} at 80 MPa, the transition temperature T_t is about 305 K, heat capacity is about 9619 J kg^{-1} K^{-1} (see Fig. S2(a) in the ESI†), and the approximately calculated adiabatic temperature change ΔT_{ad} according to eqn (1) is 22 K. Similarly, for MS, the maximum value of $\Delta S_{P_0\rightarrow P}$ is 680 J kg^{-1} K^{-1} at 60 MPa, the transition temperature T_t is about 312 K, heat capacity is about 16 313 J kg^{-1} K^{-1} (see Fig. S2(b) in the ESI†), and the approximately calculated ΔT_{ad} by eqn (1) is 13 K.[44] Because the specific heat capacity was measured by DSC at atmospheric pressure, and not under the corresponding high pressures, there should be a certain difference deviated from the actual adiabatic temperature values. Besides $\Delta S_{P_0\rightarrow P}$ and ΔT_{ad}, another important parameter for barocaloric refrigerant materials is the refrigerant capacity (RC), which can be obtained by two methods in the ESI.† In order to calculate the effective cooling capacity by Wood and Potter's method, the reversible isothermal entropy change (ΔS_r) and its δT_{FWHM} are used. In a given caloric effect system, the reversibility is confined to a certain temperature range, which relies heavily on the variation of the applied external field. As usual, the bigger the applied external field, the bigger the reversible entropy change and its full width at half-maximum. These regions can be determined by the overlap of the temperature spans during the cooling and heating processes. In this work, the RC value up to 1921 J kg^{-1} could be obtained by incorporating ΔS_r of 641 J kg^{-1} K^{-1} and the corresponding δT_{FWHM} of 3 K at 100 MPa into eqn (S4) (ESI†) for MP. Similarly, the RC value could be up to 4760 J kg^{-1} obtained by incorporating ΔS_r of 680 J kg^{-1} K^{-1} and the corresponding δT_{FWHM} of 7 K at 100 MPa into eqn (S4) (ESI†) for MS.

The other method to obtain RC is called the integration method or Gschneidner method, in which the upper and lower limit of the integration are the temperatures at the half-maximum of ΔS_r. Therefore, the RC values of MP and MS are 1442 J kg^{-1} and 4277 J kg^{-1}, respectively.

Raman spectra measurement under different pressures. To investigate the phase transition of the FAMEs, Raman spectroscopy was applied as a function of pressure and temperature. Fig. 6a and d shows the Raman spectra of the low-temperature phases and the high-temperature phases for MP and MS, respectively. It can be seen that strong peaks can be observed

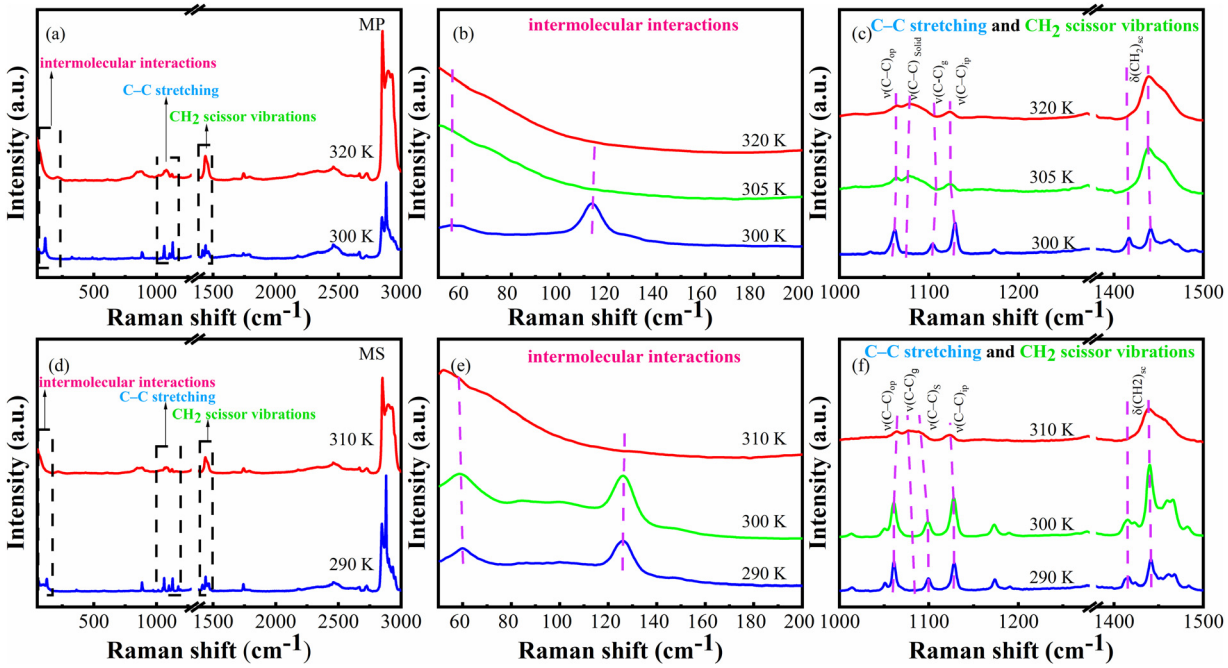

Fig. 6 Raman spectra of FAMEs in the solid phase at low temperatures and liquid phase at high temperatures. (a) For MP and (d) for MS. Temperature-dependent Raman spectra for MP in the range Raman shift $< 200\ cm^{-1}$ (b), and $1000 <$ Raman shift $< 1500\ cm^{-1}$ (c). For MS, Raman shift $< 200\ cm^{-1}$ (e), and $1000 <$ Raman shift $< 1500\ cm^{-1}$ (f).

at low frequency modes (below 200 cm^{-1}) and high frequency modes (1000–1500 cm^{-1}), which are corresponding to intermolecular interactions, C–C stretching and CH_2 scissor vibrations, respectively.[48,49] For low frequency modes (below 200 cm^{-1}), the peaks are relevant to intermolecular interactions. It can be seen in Fig. 6b and e that MP has two bands at 56 and 113 cm^{-1} and MS has two bands at 60 and 126 cm^{-1}, respectively for the low temperature phase (solid state phase here). With the increase of temperature, the bands disappear for both MP and MS, which means solid–liquid transition has happened, and the materials become a liquid phase. For the high-frequency mode (1000–1500 cm^{-1}), it can be seen in Fig. 6c and f that the bands at 1061 cm^{-1} (out-of-phase aliphatic C–C stretch all-*trans*, $\nu(C–C)_{op}$) and 1129 cm^{-1} (in-phase aliphatic C–C stretch all-*trans*, $\nu(C–C)_{ip}$) of both MP and MS are weaker and broader with the increase of temperature. Similarly, as the temperature increases, the band at 1104 cm^{-1} (aliphatic C–C stretch all-*trans*, ν(C–C) solid) for MP and the band at 1099 cm^{-1} (aliphatic C–C stretch all-*trans*, ν(C–C) solid) for MS disappeared, respectively. In contrast, the band at 1080 cm^{-1} (aliphatic C–C stretch of the *gauche* segment, $\nu(C–C)_g$) appears at high temperatures, which couldn't be observed at low temperatures. Also, wave numbers 1417 and 1441 cm^{-1} in Fig. 6c and 1416 and 1441 cm^{-1} in Fig. 6f correspond to scissor deformations ($\delta(CH_2)_{sc}$) for MP and MS, respectively, which become broader with the increase of temperature. Therefore, it can be judged from the Raman spectra shown in Fig. 6 that the *trans* bond in the solid and *gauche* bond in the liquid phase are the most obviously different structures between these two states.

As shown in Fig. 7, it can be seen that the Raman spectra of both MP and MS are similar and both were accompanied by an

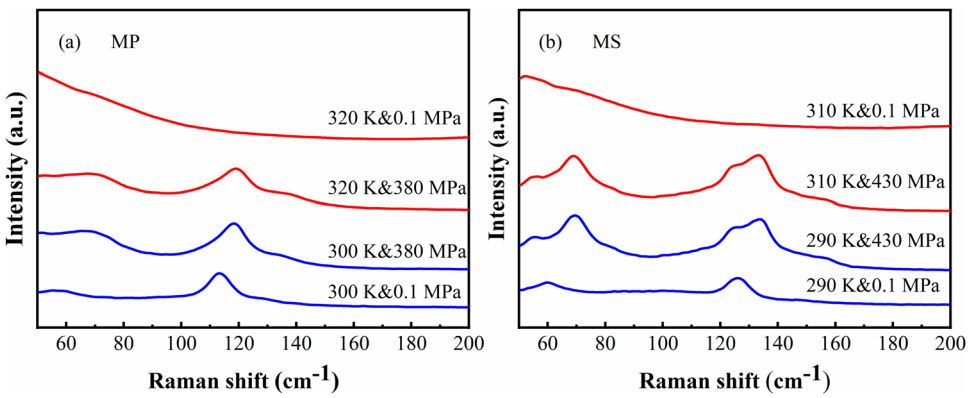

Fig. 7 Pressure-dependent Raman spectra of MP at 300 and 320 K (a) and 290 K and 310 K for MS (b).

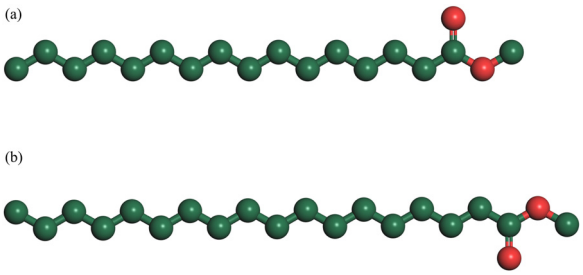

Fig. 8 Schematic diagram of the structures of (a) methyl palmitate (MP) and (b) methyl stearate (MS).

obvious pressure-induced blue shift of peak positions. And the peak located at 126 cm^{-1} will be split into two superposed peaks (124.5 and 133.5 cm^{-1}) for the solid state phase of MS at 298 K when the pressure was increased to 430 MPa, indicative of the phase transition in the solid state.[50] Also, for the liquid phase at 310 K, well-defined peaks out of the featureless spectrum under ambient pressure will be induced at a certain external pressure just as shown in Fig. 7b, as a verification of the pressure induced phase transitions from liquid state to solid state. This also indicates that the phase transitions can be tuned by both temperature and pressure.

Fig. 8 is the schematic structure of MP and MS under atmospheric pressure. It can be seen that both of them are connected by all-*trans* bonds. When the temperature increases, *trans* bonds are converted into *gauche* bonds. This process does not cause the C–C–C bond to change, but brings about rotations of the C–C bond, resulting in an increase in configurational entropy. In general, the increase of pressure will limit the rotation angles, which will affect the number of *gauche* bonds and the configuration entropy.

Fig. 9 is the schematic structure of MP in the liquid state. It can be seen that it is connected by *gauche* bonds. When the temperature decreases, the *gauche* bonds are converted into *trans* bonds. This process does not cause the C–C–C bond to change, but brings about rotation of the C–C bond, resulting in an decrease in configurational entropy. In organic molecules, the conformations are recorded as innumerable specific images of atoms or groups arranged in space generated by the rotation of single C–C bonds. A complete rotation of a single C–C bond has three potential minima which are a *trans* form and two *gauche* forms obtainable from the *trans* form by internal rotation of ±120°. As usual, the *gauche* bonds have a higher energy than the *trans* bond. In general, the increase of pressure will limit the rotation angles, which will affect the number of *gauche* bonds and the configuration entropy. As shown in Fig. 8, it can be seen that *gauche* bonds are decreased when pressure increases for the high-temperature phase, which is similar to the situation in pressure-induced liquid–solid phase transition.

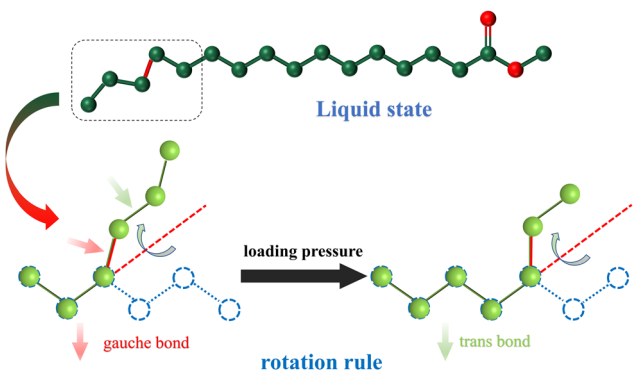

Fig. 9 Schematic diagram of the structure of the methyl palmitate in the liquid state and the rotation rules for the *trans* bond and *gauche* bond under loading pressure.

Conclusions

The barocaloric effect of MP and MS has been discovered, revealing a dramatic impact with a maximum isothermal entropy change of up to 707 J kg^{-1} K^{-1} at 80 MPa for MP, and 680 J kg^{-1} K^{-1} at 60 MPa for MS, respectively. Both MP and MS exhibit reversible entropy changes of 641 J kg^{-1} K^{-1} and 680 J kg^{-1} K^{-1}. Raman spectroscopy has confirmed the solid-to-liquid transitions induced by temperature and pressure at transition temperatures. The barocaloric effect, pressure sensitivity, large refrigeration capacity, and minimal thermal hysteresis of a few kelvin position FAMEs as strong contenders for room-temperature barocaloric refrigeration.

Author contributions

Diyi Fu: data curation (equal); formal analysis (equal); investigation (equal); methodology (equal); writing – original draft (equal); writing – review & editing (equal). Xiu Su: formal analysis (equal); investigation (equal); methodology (equal). Haoyu Wang: investigation (equal); validation (equal). Zhenxing Li: supervision (equal). Qiang Zheng: conceptualization (equal); supervision (equal); writing – review & editing (equal). Jun Shen: resources (equal). Bing Li: resources (equal). Juan Du: conceptualization (equal); supervision (equal); writing – review & editing (equal).

Data availability

The data that support the findings of this study are available from the corresponding author upon reasonable request.

Conflicts of interest

The authors declare no competing financial interest.

Acknowledgements

This work was financially supported by the National Key Research and Development Program of China (No. 2023YFB3507600) and National Natural Science Foundation of China (No. U23A20549 and 52171184).

References

1 Low-carbon heating and cooling: Overcoming one of world's most important net zero challenges (climate change: Science and solutions, June 2021), https://royalsociety.org/-/media/policy/projects/climate-change-sciencesolutions/climate-science-solutions-heating–cooling.pdf.

2 B. Li, Y. Kawakita, S. Ohira-Kawamura, T. Sugahara, H. Wang, J. Wang, Y. Chen, S. I. Kawaguchi, S. Kawaguchi and K. Ohara, *et al.*, Colossal barocaloric effects in plastic crystals, *Nature*, 2019, **567**(7749), 506–510.

3 M. O. McLinden, J. S. Brown, R. Brignoli, A. F. Kazakov and P. A. Domanski, Limited options for low-global-warming-potential refrigerants, *Nat. Commun.*, 2017, **8**, 14476.

4 X. She, L. Cong, B. Nie, G. Leng, H. Peng, Y. Chen, X. Zhang, T. Wen, H. Yang and Y. Luo, Energy-efficient and -economic technologies for air conditioning with vapor compression refrigeration: A comprehensive review, *Appl. Energy*, 2018, **232**, 157–186.

5 P. C. Stern, K. B. Janda, M. A. Brown, L. Steg, E. L. Vine and L. Lutzenhiser, Opportunities and insights for reducing fossil fuel consumption by households and organizations, *Nat. Energy*, 2016, **1**(5), 16043.

6 G. J. Velders, D. W. Fahey, J. S. Daniel, M. McFarland and S. O. Andersen, The large contribution of projected HFC emissions to future climate forcing, *Proc. Natl. Acad. Sci. U. S. A.*, 2009, **106**(27), 10949–10954.

7 S. A. Montzka, B. D. Hall and J. W. Elkins, Accelerated increases observed for hydrochlorofluorocarbons since 2004 in the global atmosphere, *Geophys. Res. Lett.*, 2009, **36**(3), L03804.

8 A. Stohl, P. Seibert, J. Arduini, S. Eckhardt, P. Fraser, B. R. Greally, C. Lunder, M. Maione, J. Mühle and S. O'Doherty, *et al.*, An analytical inversion method for determining regional and global emissions of greenhouse gases: Sensitivity studies and application to halocarbons, *Atmos. Chem. Phys.*, 2009, **9**(5), 1597–1620.

9 P. Purohit, L. Höglund-Isaksson, J. Dulac, N. Shah, M. Wei, P. Rafaj and W. Schöpp, Electricity savings and greenhouse gas emission reductions from global phase-down of hydrofluorocarbons, *Atmos. Chem. Phys.*, 2020, **20**(19), 11305–11327.

10 A. Henry, R. Prasher and A. Majumdar, Five thermal energy grand challenges for decarbonization, *Nat. Energy*, 2020, **5**(9), 635–637.

11 P. Lloveras and J.-L. Tamarit, Advances and obstacles in pressure-driven solid-state cooling: A review of barocaloric materials, *MRS Energy Sustainability*, 2021, **8**, 3–15.

12 L. Mañosa and A. Planes, Solid-state cooling by stress: A perspective, *Appl. Phys. Lett.*, 2020, **116**(5), 050501.

13 K. A. GschneidnerJr, V. K. Pecharsky and A. O. Tsokol, Recent developments in magnetocaloric materials, *Rep. Prog. Phys.*, 2005, **68**(6), 1479–1539.

14 V. Franco, J. S. Blázquez, J. J. Ipus, J. Y. Law, L. M. Moreno-Ramírez and A. Conde, Magnetocaloric effect: From materials research to refrigeration devices, *Prog. Mater. Sci.*, 2018, **93**, 112–232.

15 G. V. Brown, Magnetic heat pumping near room temperature, *J. Appl. Phys.*, 1976, **47**(8), 3673–3680.

16 D. Cong, W. Xiong, A. Planes, Y. Ren, L. Manosa, P. Cao, Z. Nie, X. Sun, Z. Yang, X. Hong and Y. Wang, Colossal Elastocaloric Effect in Ferroelastic Ni-Mn-Ti Alloys, *Phys. Rev. Lett.*, 2019, **122**(25), 255703.

17 X. Liu, Z. Wu, T. Guan, H. Jiang, P. Long, X. Li, C. Ji, S. Chen, Z. Sun and J. Luo, Giant room temperature electrocaloric effect in a layered hybrid perovskite ferroelectric: $[(CH_3)_2CHCH_2NH_3]_2PbCl_4$, *Nat. Commun.*, 2021, **12**(1), 5502.

18 B. Neese, B. Chu, S. G. Lu, Y. Wang, E. Furman and Q. M. Zhang, Large electrocaloric effect in ferroelectric polymers near room temperature, *Science*, 2008, **321**(5890), 821–823.

19 A. S. Mischenko, Q. Zhang, J. F. Scott, R. W. Whatmore and N. D. Mathur, Giant electrocaloric effect in thin-film $PbZr_{0.95}Ti_{0.05}O_3$, *Science*, 2006, **311**(5765), 1270–1271.

20 X. Su, Z. Zhang, J. Liu, Q. Zheng, Z. Li, J. Shen, B. Li and J. Du, Colossal Barocaloric Effect of Binary Fatty Acid Methyl Esters under Low Pressures near Room Temperature, *J. Phys. Chem. Lett.*, 2024, **15**(7), 1962–1968.

21 Z. Zhang, T. Xiong, Z. Zhang, B. Li, P. Tong, J. Shen, Q. Zheng and J. Du, Colossal Barocaloric Effect near Ambient Temperature in 1-Dodecanol under a Low Pressure, *J. Phys. Chem. Lett.*, 2024, **15**(28), 7141–7146.

22 J. Seo, R. Ukani, J. Zheng, J. D. Braun, S. Wang, F. E. Chen, H. K. Kim, S. Zhang, C. Thai and R. D. McGillicuddy, *et al.*, Barocaloric Effects in Dialkylammonium Halide Salts, *J. Am. Chem. Soc.*, 2024, **146**(4), 2736–2747.

23 P. Lloveras, A. Aznar, M. Barrio, P. Negrier, C. Popescu, A. Planes, L. Manosa, E. Stern-Taulats, A. Avramenko and N. D. Mathur, *et al.*, Colossal barocaloric effects near room temperature in plastic crystals of neopentylglycol, *Nat. Commun.*, 2019, **10**(1), 1803.

24 Y. Kosugi, M. Goto, Z. Tan, A. Fujita, T. Saito, T. Kamiyama, W. T. Chen, Y. C. Chuang, H. S. Sheu, D. Kan and Y. Shimakawa, Colossal Barocaloric Effect by Large Latent Heat Produced by First-Order Intersite-Charge-Transfer Transition, *Adv. Funct. Mater.*, 2021, **31**(25), 2009476.

25 D. Boldrin, Fantastic barocalorics and where to find them, *Appl. Phys. Lett.*, 2021, **118**(17), 170502.

26 Y. Gao, H. Liu, F. Hu, H. Song, H. Zhang, J. Hao, X. Liu, Z. Yu, F. Shen and Y. Wang, *et al.*, Reversible colossal barocaloric effect dominated by disordering of organic chains in $(CH_3–(CH_2)_{n-1}–NH_3)_2MnCl_4$ single crystals, *NPG Asia*, *Materials*, 2022, **14**(1), 34.

27 M. V. Gorev, E. A. Mikhaleva, I. N. Flerov and E. V. Bogdanov, Conventional and inverse barocaloric effects in ferroelectric NH4HSO4, *J. Alloys Compd.*, 2019, **806**, 1047–1051.

28 W. J. Xu, Y. Zeng, W. Yuan, W. X. Zhang and X. M. Chen, A large room-temperature entropy change in a new hybrid ferroelastic with an unconventional bond-switching mechanism, *Chem. Commun.*, 2020, **56**(69), 10054–10057.

29 J. Min, A. K. Sagotra and C. Cazorla, Large barocaloric effects in thermoelectric superionic materials. *Physical Review*, *Materials*, 2020, **4**(1), 015403.

30 R. Li, Z. Zhang and Y. S. Bibik, Gural'skiy, I. y. A.; Zatovsky, I. V.; Liu, Z.; Li, Q.; Li, B.; Levchenko, G.; Liu, B. Colossal barocaloric effect of the spin-crossover compound

{Fe(pz)$_2$(BH$_3$CN)$_2$} near room temperature, *Appl. Phys. Lett.*, 2024, **124**(12), 122202.

31 H. G. Ramírez-Hernández, A. Morales-Fuentes, F. A. Sánchez-Cruz, S. Méndez-Díaz, H. D. García-Lara and S. Martínez-Martínez, Experimental study on the operating characteristics of a display refrigerator phasing out R134a to R1234ze(E) and its binary blends, *Int. J. Refrig.*, 2022, **138**, 1–12.

32 M. Gelpi, J. Garcia-Ben, S. Rodriguez-Hermida, J. Lopez-Beceiro, R. Artiaga, A. Baalina, M. Romero-Gomez, J. Romero-Gomez, S. Zaragoza and J. Salgado-Beceiro, *et al.*, Empowering CO_2 Eco-Refrigeration With Colossal Breathing-Caloric-Like Effects in MOF-508b, *Adv. Mater.*, 2024, **36**(16), e2310499.

33 J. Lin, P. Tong, K. Zhang, K. Tao, W. Lu, X. Wang, X. Zhang, W. Song and Y. Sun, Colossal and reversible barocaloric effect in liquid-solid-transition materials n-alkanes, *Nat. Commun.*, 2022, **13**(1), 596.

34 C. Zhang, D. Wang, S. Qian, Z. Zhang, X. Liang, L. Wu, L. Long, H. Shi and Z. Han, Giant barocaloric effects with a wide refrigeration temperature range in ethylene vinyl acetate copolymers, *Mater. Horiz.*, 2022, **9**(4), 1293–1298.

35 M. M. Kenisarin, Thermophysical properties of some organic phase change materials for latent heat storage. A review, *Sol. Energy*, 2014, **107**, 553–575.

36 D. G. Atinafu, Y. S. Ok, H. W. Kua and S. Kim, Thermal properties of composite organic phase change materials (PCMs): A critical review on their engineering chemistry, *Appl. Therm. Eng.*, 2020, **181**, 115960.

37 K. Zhang, R. Song, J. Qi, Z. Zhang, Z. Zhang, C. Yu, K. Li, Z. Zhang and B. Li, Colossal Barocaloric Effect in Carboranes as a Performance Tradeoff, *Adv. Funct. Mater.*, 2022, **32**(20), 2112622.

38 F. B. Li, M. Li, X. Xu, Z. C. Yang, H. Xu, C. K. Jia, K. Li, J. He, B. Li and H. Wang, Understanding colossal barocaloric effects in plastic crystals, *Nat. Commun.*, 2020, **11**(1), 4190.

39 A. Aznar, P. Lloveras, M. Romanini, M. Barrio, J. L. Tamarit, C. Cazorla, D. Errandonea, N. D. Mathur, A. Planes, X. Moya and L. Manosa, Giant barocaloric effects over a wide temperature range in superionic conductor AgI, *Nat. Commun.*, 2017, **8**(1), 1851.

40 Y. H. Gao, D. H. Wang, F. X. Hu, Q. Z. Huang, Y. T. Song, S. K. Yuan, Z. Y. Tian, B. J. Wang, Z. B. Yu and H. B. Zhou, *et al.*, Low pressure reversibly driving colossal barocaloric effect in two-dimensional vdW alkylammonium halides, *Nat. Commun.*, 2024, **15**(1), 1838.

41 C. Yu, J. Huang, J. Qi, P. Liu, D. Li, T. Yang, Z. Zhang and B. Li, Giant barocaloric effects in formamidinium iodide, *APL Mater.*, 2022, **10**(1), 011109.

42 K. Lunser, E. Kavak, K. Gurpinar, B. Emre, O. Atakol, E. Stern-Taulats, M. Porta, A. Planes, P. Lloveras, J. L. Tamarit and L. Manosa, Elastocaloric, barocaloric and magnetocaloric effects in spin crossover polymer composite films, *Nat. Commun.*, 2024, **15**(1), 6171.

43 J. Seo, R. D. McGillicuddy, A. H. Slavney, S. Zhang, R. Ukani, A. A. Yakovenko, S. L. Zheng and J. A. Mason, Colossal barocaloric effects with ultralow hysteresis in two-dimensional metal-halide perovskites, *Nat. Commun.*, 2022, **13**(1), 2536.

44 J. Li, D. Dunstan, X. Lou, A. Planes, L. Mañosa, M. Barrio, J.-L. Tamarit and P. Lloveras, Reversible barocaloric effects over a large temperature span in fullerite C60, *J. Mater. Chem. A*, 2020, **8**(39), 20354–20362.

45 T. Xiong, J. Lin, T. Zhou, G. Shi, T. Ye, X. Pan, K. Liu, R. Jiang, R. Zhang and W. Song, Colossal barocaloric effect of phase-change fatty acids, *Appl. Phys. Lett.*, 2024, **125**(6), 061903.

46 M. Seredyuk, R. Li, K. Znovjyak, Z. Zhang, F. J. Valverde-Muñoz, B. Li, M. C. Muñoz, Q. Li, B. Liu, G. Levchenko and J. A. Real, Reversible Colossal Barocaloric Effect of a New FeII Molecular Complex with Low Hysteretic Spin Crossover Behavior, *Adv. Funct. Mater.*, 2024, **34**, 30.

47 X. Wang, H. Xuan, M. Ji, F. Chen, Z. Han, P. Han and J. Qiao, Large barocaloric and magnetocaloric effects in $MnFe_{0.8+x}$-$Ni_{1.2-x}$SiGe0.5 high-entropy intermetallics, *Appl. Phys. Lett.*, 2024, **124**(9), 092411.

48 J. R. Beattie, S. E. Bell and B. W. Moss, A critical evaluation of Raman spectroscopy for the analysis of lipids: fatty acid methyl esters, *Lipids*, 2004, **39**(5), 407–419.

49 A. M. Miranda, E. W. Castilho-Almeida, E. H. Martins Ferreira, G. F. Moreira, C. A. Achete, R. A. S. Z. Armond, H. F. Dos Santos and A. Jorio, Line shape analysis of the Raman spectra from pure and mixed biofuels esters compounds, *Fuel*, 2014, **115**, 118–125.

50 A. Francisco-López, B. Charles, O. J. Weber, M. I. Alonso, M. Garriga, M. Campoy-Quiles, M. T. Weller and A. R. Goñi, Pressure-Induced Locking of Methylammonium Cations versus Amorphization in Hybrid Lead Iodide Perovskites, *J. Phys. Chem. C*, 2018, **122**(38), 22073–22082.